Chemical Engineering Journal 476 (2023) 146488

Contents lists available at ScienceDirect

Chemical Engineering Journal

journal homepage: www.elsevier.com/locate/cej

Tandem photocatalytic production of H_2O_2 and propylene oxide on 5-Bromoisatin modified carbon nitride

Xinyu Wang [a,1], Pei Zhou [a,1], Qiang Zhou [a], Qinhua Zhang [a], Hui Ning [a], Mingbo Wu [a,*], Wenting Wu [a,*]

[a] State Key Laboratory of Heavy Oil Processing, College of Chemistry and Chemical Engineering & Institute of New Energy, China University of Petroleum (East China), Qingdao 266580, PR China

ARTICLE INFO

Keywords:
Photocatalytic H_2O_2 production
Ligand doping
TS-1
Propylene epoxidation
Tandem reaction

ABSTRACT

Propylene oxide (PO) is an important raw material and synthetic intermediate for organic chemical synthesis. The direct in-situ synthesis of hydrogen peroxide (H_2O_2) using molecular oxygen to produce PO is considered as one of the most promising methods. Herein, we propose a photocatalytic multiphase system for the production of PO with oxygen. The ligand 5-bromoindoline-2,3-dione doped graphitic carbon nitride (CN/Bd) was employed as a photocatalyst for the in-situ production of H_2O_2, in tandem with epoxidation catalyst titanium silicalite-1 (TS-1) to achieve the epoxidation of propylene. This system achieved H_2-free and efficient production of PO at room temperature with a high yield of 1.33 $mmol \cdot g^{-1} \cdot h^{-1}$, the selectivity of PO over 99% and H_2O_2 utilization efficiency over 95%. The combination of in-situ H_2O_2 generation and selective oxidation reaction realizes the efficient utilization of H_2O_2 and provides guidance for safer industrial production of PO.

1. Introduction

As an important basic chemical raw material for the production of polyether polyol, propylene glycol and various non-ionic surfactants, propylene oxide (PO) is the third largest propylene derivative after polypropylene and acrylonitrile [1–3]. In 2021, China's PO production was about 3.46 million tons, while its apparent demand was about 3.89 million tons. With the development of downstream polyurethane industry, the PO demand will continue to grow in the next few years [4]. However, China's current production capacity still fails to keep up with the demand of its domestic market, and needs to import PO from other countries. Compared with pollution intensive production processes of PO (the chlorohydrin method and the co-oxidation method) [5,6], hydrogen peroxide (H_2O_2) oxidation method overcomes the disadvantages of complex production process, serious environmental pollution, high operating pressure and serious equipment corrosion [7]. Therefore, the propylene epoxidation process with H_2O_2 as oxidant (hydrogen peroxide/propylene oxide, HPPO) has attracted great attention [8,9], which has high conversion and selectivity, only 30% of the wastewater volume and 65% of the energy consumption of other existing technologies [10].

As an effective oxidant for PO production, H_2O_2 is mainly produced via the anthraquinone route. This path can produce high concentrations of H_2O_2, but there are certain safety and economic problems during transportation and storage. Many achievements have been achieved in epoxidation reactions using in situ-generated H_2O_2 [7,11,12]. Feng et al. deposited gold-silver bimetallic catalysts on titanium silicalite-1 (TS-1), which first synthesized H_2O_2 from H_2 and O_2 at the gold-silver bimetallic site, and then H_2O_2 reacted with propylene at the nearby Ti^{4+} site to produce PO [13]. However, there are some problems with the noble metal doping, such as high operation costs and high explosion risk [14,15]. Therefore, developing a low-cost catalyst for in-situ synthesis of H_2O_2 using molecular oxygen and H_2-free under mild conditions, and then reacts in tandem with titanium silicate-1 for PO production seems to be a good strategy.

In recent years, photocatalytic H_2O_2 production has attracted extensive attention due to its H_2-free and environmentally friendly process [16–18]. Several semiconductor materials have been developed for the photocatalytic production of H_2O_2 [19], such as TiO_2 [20,21], g-C_3N_4 [22,23] and $BiVO_4$ [24], etc. Noteworthily, many studies mainly focus on improving the yield of H_2O_2, while ignoring the in-situ utilization of H_2O_2 synthesized by photocatalysis. Although in-situ

* Corresponding authors.
E-mail addresses: wumb@upc.edu.cn (M. Wu), wuwt@upc.edu.cn (W. Wu).
[1] These authors contributed equally to this work.

https://doi.org/10.1016/j.cej.2023.146488
Received 14 July 2023; Received in revised form 8 September 2023; Accepted 5 October 2023
Available online 10 October 2023

decomposition of H_2O_2 to ·OH has been reported for environmental remediation and sterilization, little attention has been paid to its use for selective oxidation of hydrocarbons.

Herein, we proposed a tandem strategy to achieve the photocatalytic synthesis and in-situ utilization of H_2O_2 in propylene epoxidation. The 5-bromoindole-2, 3-dione was doped into g-C_3N_4 (CN/Bd) by ligand doping strategy, mixed with titanium silicate-1 (TS-1) heterogeneous catalyst to realize epoxidation of propylene under mild conditions without any H_2 or electrical energy. The selectivity of the product PO exceeded 99%, efficiently utilizing the in situ-generated H_2O_2.

2. Experimental

2.1. Catalyst synthesis

2.1.1. Synthesis of g-C_3N_4 (CN)

10.00 g of melamine were annealed at 400 °C with a heating rate of 3 °C min^{-1} for 4 h in a muffle furnace. After cooling down naturally, the resulting white solid was washed three times and dried in a vacuum at 60 °C overnight to obtain melem.

Then, 2.00 g of melem were further calcined at 550 °C with a heating rate of 5 °C min^{-1} for 4 h in a muffle furnace. After cooling down naturally, the resulting yellowish solid was washed three times and dried in a vacuum at 60 °C overnight. The prepared sample (g-C_3N_4) was denoted as CN.

2.1.2. Synthesis of CN/Bd

500 mg of melem and certain amount of 5-bromoindoline-2,3-dione (Bd) were mixed well with a mortar and pestle. Subsequently, the mixture was placed in a tubular furnace and heated at 550 °C for 4 h with a heating rate of 5 °C min^{-1}. After natural cooling, the resulting brown solid was washed three times and dried overnight and denoted as CN/Bd-X. The CN/Bd-X (X = 1, 5, 7, 10 mg) photocatalysts with different Bd content was prepared under the same conditions, where X represents the added amounts of Bd.

2.1.3. Synthesis of titanium silicalite-1 (TS-1) and pure-silica silicalite-1 (S-1)

17.00 g of tetrapropylammonium hydroxide solution, 21.45 g of deionized water, 30.44 g of tetraethyl orthosilicate and 0.25 g of tetrabutyl titanate were mixed completely. Subsequently, the mixed solution was irradiated by ultraviolet light (500 W, mercury lamp) for 1 h, and then the transparent solution was transferred into a Teflon-lined stainless autoclave to crystallize at 170 °C for three days. The as-synthesized product was washed for several times and dried at 80 °C. The sample was calcined at 550 °C for 4 h in air at a heating rate of 4 °C min^{-1} to remove the template and obtain white powder, denoted as TS-1 [25]. The pure-silica silicalite-1 (S-1) was synthesized using the same procedure, except that no titanium source was added.

2.2. Photocatalytic evaluation

2.2.1. H_2O_2 production

All photocatalytic H_2O_2 production experiments have been carried out in the custom-made photochemical vial (10 mL) and a blue light lamp (10 W) with a wavelength of 420–430 nm was used as the light source [26]. Typically, 3 mg of photocatalyst was dispersed in 2 mL of methanol aqueous solution (V_{MeOH}: V_{H2O} = 1:1), then the suspension was ultrasonically dispersed for 5 min. Next, oxygen was continuously bubbled into the suspension for 30 min and stirred for 30 min under dark condition to achieve adsorption–desorption equilibrium. After that, the reaction solution was taken at intervals under blue light irradiation and the concentrations were detected sequentially.

2.2.2. H_2O_2 detection

The concentration of H_2O_2 was detected by the UV spectrophotometer (model Shimadzu UV2700). Under acidic conditions, H_2O_2 can react with potassium titanium oxalate to produce the orange pertitanate complex, which can be detected by the UV spectrophotometer with a peak of 400 nm. The absorbance produced by pertitanate is proportional to the H_2O_2 concentration.

Different volume (0.2, 0.4, 0.6, 0.8, 1.0, 1.2 mL) of 2 mM H_2O_2 solution was taken in a flask containing 0.5 mL of 3 M sulfuric acid and 0.5 mL of 0.05 M titanium potassium oxalate, followed by the addition of water to 5 mL, and the absorbance was measured after 10 min. The equation between absorbance and H_2O_2 concentration was obtained (Eq. (1). The standard curve is shown in **Fig. S1**, where Y is the H_2O_2 concentration (mmol L^{-1}) and X is the absorbance.

$$Y = 1.03X + 0.002 \ (R^2 = 0.9998) \tag{1}$$

Typically, 1 mL of the filtered reaction solution was added to mixed solution containing 0.5 mL of 3 M sulfuric acid and 0.5 mL of 0.05 M titanium potassium oxalate, followed by the addition of 3 mL of water. The absorbance was measured after 10 min and the concentration of H_2O_2 in the reaction solution was obtained according to the above equation.

$$H_2O_2 conv. = \frac{n^0_{H_2O_2} - n_{H_2O_2}}{n^0_{H_2O_2}} \times 100\% \tag{2}$$

$$H_2O_2 eff. = \frac{n_{PO}}{n^0_{H_2O_2} - n_{H_2O_2}} \times 100\% \tag{3}$$

H_2O_2 conv. and H_2O_2 eff. stand for the conversion and utilization efficiency of H_2O_2, respectively. $n^0_{H_2O_2}$ and $n_{H_2O_2}$ stand for the initial and final mole content of H_2O_2, respectively. n_{PO} stand for the numbers of moles of PO.

2.2.3. PO production

The PO production experiments were carried out under the same conditions as photocatalytic H_2O_2 production experiments. Typically, 5 mg of photocatalyst and 5 mg of TS-1 were dispersed in 2 mL of methanol aqueous solution (V_{MeOH}: V_{H2O} = 1:1), then the suspension was ultrasonically dispersed for 5 min. Next, oxygen was continuously bubbled into the suspension for 30 min and stirred for 30 min under dark condition to achieve adsorption–desorption equilibrium. In addition, 10 mL of oxygen and 10 mL of propylene were injected into the reaction vial by using a 10 mL syringe. After that, a blue LED light lamp (10 W) with a wavelength of 420–430 nm was used as light source. The product yield of PO was detected using gas chromatography.

2.2.4. PO detection

After the reaction, the liquid products were filtered with a 0.22 μm syringe filter (HR70003, Prismatic) and analyzed with a gas chromatograph (GC 9790plus) equipped with the flame ionization detectors (FID) and the KB624 (30 m × 320 μm × 0.25 μm) column. The products were quantified according to the internal standard method with acetonitrile as an internal standard.

2.3. Characterization

The X-ray diffraction (XRD) pattern was performed using X'Pert PRO MPD (Netherlands) in Cu Kα radiation source, in the diffraction angle (2θ) range of 5–75°. Scanning electron microscopy (SEM) images were taken on the Hitachi S-4800. Transmission electron microscopy (TEM) images were collected on JEM-2100UHR. X-ray photoelectron spectroscopy (XPS) measurements were performed on Escalab 250Xi (Thermo Fisher). Fourier Transform Infrared Spectra (FT-IR) were recorded on Thermo Nicolet nexus over 4000–400 cm^{-1}. Ultraviolet–visible (UV–vis) diffuse reflectance spectra were obtained from the dry-pressed disk samples using a scan UV–vis spectrophotometer (UV-2700, Shimadzu) equipped with an integrating sphere, using $BaSO_4$

as a reflectance sample. Photoluminescence Spectroscopy (PL) spectra were recorded on RF-6000 (Shimadzu) with an exciton wavelength of 365 nm. Electron paramagnetic resonance (EPR) spectra using 5,5-dimethyl-L-pyrroline-N-oxide (DMPO) as spin trap reagent, were measured on a JES-X320 spectrometer in dark or under visible light irradiation ($\lambda > 420$ nm). Photoelectrochemical measurements including photocurrent density, electrochemical impedance spectroscopy (EIS) and Mott-Schottky (M−S) plots were conducted with CHI 660E (Chenhua) work-station with the traditional three-electrode cell system (Pt sheet as counter electrode, Ag/AgCl electrode as reference electrode, samples as working electrode).

3. Results and discussion

3.1. Synthesis and structural characterizations of CN/Bd and TS-1

In order to achieve the epoxidation of propylene with O_2, the whole reaction should be carried out by two catalysts: the photocatalyst for the selective reduction of O_2 into H_2O_2 and the TS-1 for the activation of H_2O_2 to achieve the propylene epoxidation. As shown in Fig. 1**a**, the photocatalyst was synthesized by a two-step calcination method. The precursor melamine was first calcined at 400 °C to obtain the melem intermediate, which was then combined with the ligand Bd to obtain the final samples. The titanium silicate-1 (TS-1) zeolite was synthesized according to the previous report [25].

SEM and TEM images were performed to reveal the morphologies of catalysts. As shown in Fig. 1**b, c**, the irregular rod-like structure of g-C_3N_4 disrupted upon the introduction of the Bd molecule, leading to a partial collapse and gradual aggregation into fragmented forms. Further evidence came from TEM images (Fig. 1**d, e**). CN/Bd exhibited a multilayer lamellar structure compared with pristine CN. This increased multilayer structure may be beneficial to increase the activity of CN/Bd by increasing its adsorption activation site to O_2 or substrates.

The crystal and phase structure of CN/Bd with incorporation of different Bd content were investigated by XRD measurements. As shown in **Fig. S2**, two prominent peaks at 12.8° and 27.6° attributed to (1 0 0) and (0 0 2) facets were observed for CN, representing the in-plane structural stacking of the triple homogeneous triazine unit ring of g-C_3N_4 and the interlayer diffraction of graphitic phase structure [27–29], respectively. However, the peaks intensity of CN/Bd gradually becomes broader and weaker with the incorporation of more Bd group (Fig. 2**a**), suggesting that the presence of the Bd group may influence the crystalline characteristics of g-C_3N_4. The (1 0 0) peak gradually decrease, which is attributed to the substitution of the *tert*-N-H in g-C_3N_4 structure by Bd group, leading to a decrease in the structural periodicity of the 3-s-triazine ring within the layer. Besides, the weaker (0 0 2) peak of CN/Bd is assigned to the fact that the incorporation of Bd inhibit stacking of aromatic system to form thinner lamellae, suggesting the decreased crystallinity of the g-C_3N_4 structure induced by doping of Bd. This effect may favor the activity of CN/Bd by increasing the surface active site of catalyst, promoting visible-light absorption and photogenerated carrier separation [30].

FT-IR measurement was conducted to investigate the chemical states of catalysts. As shown in Fig. 2**b**, the peaks were observed on CN and CN/Bd at 810 cm^{-1}, 1200–1650 cm^{-1} and 3000–3500 cm^{-1}, corresponding to the bending vibration of graphitic carbon nitride triazine

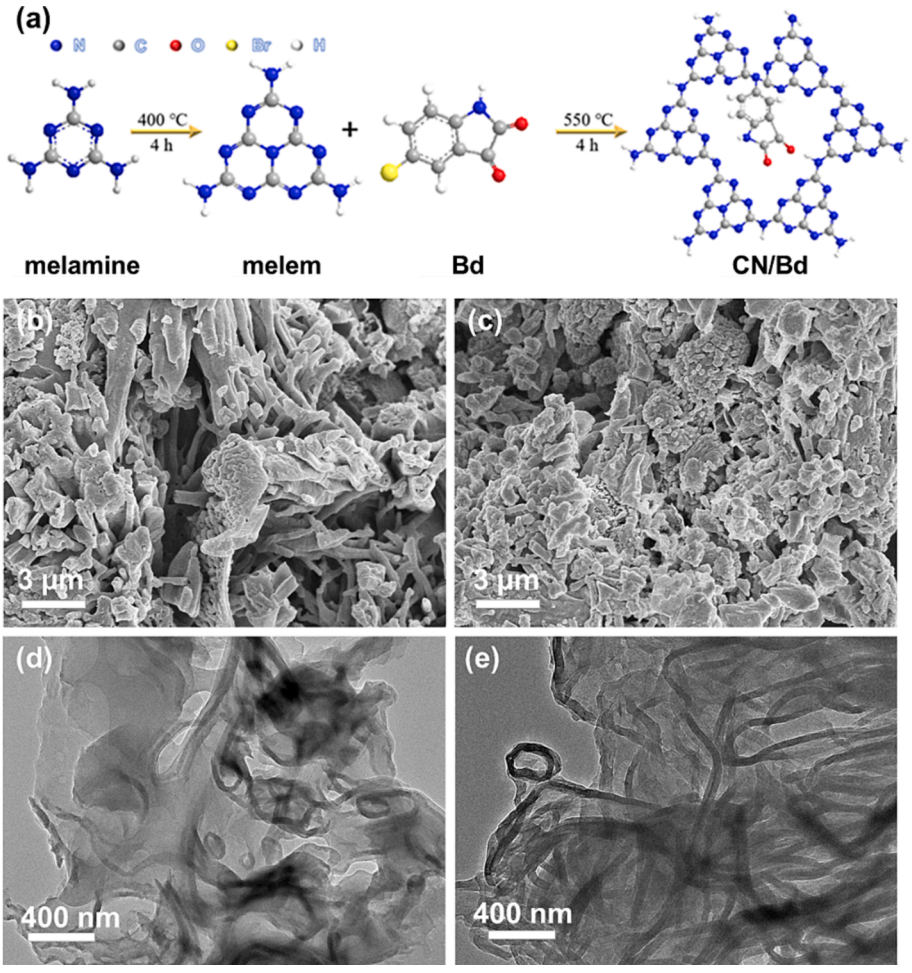

Fig. 1. (a) Two-step synthetic procedure of photocatalyst CN/Bd-X, (b-c) SEM images and (d-e) TEM images of CN and CN/Bd.

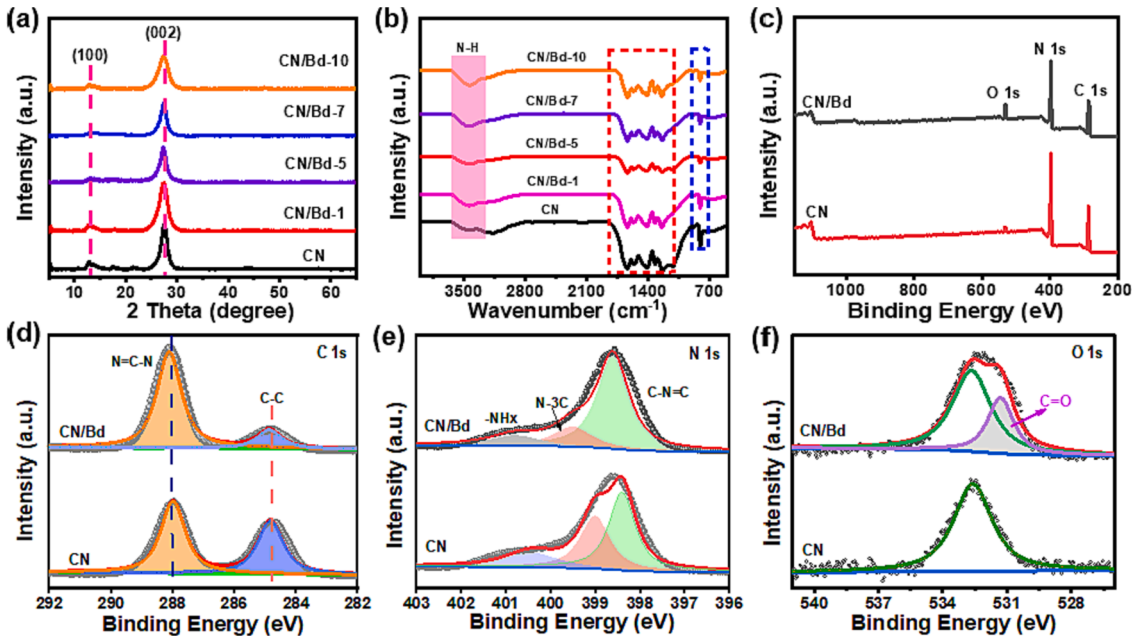

Fig. 2. (a) XRD patterns and (b) FT-IR spectra of CN and CN/Bd-X, (c) total XPS spectra and (d-f) C 1 s, N 1 s and O 1 s XPS spectra of CN and CN/Bd.

rings, the C-N and C = N stretching vibrations of heterocyclic aromatic groups, and the stretching vibrations of N-H and O-H bonds [31], respectively. It indicates that CN/Bd still retains the basic structure of g-C_3N_4. Notably, the peak intensity of CN/Bd at 3400 cm^{-1} is higher than that of CN. Combined with the FT-IR spectrum of the Bd molecule (Fig. S3), the characteristic peak at 3400 cm^{-1} could be attributed to the stretching vibration of the amino group in the Bd molecule. In addition, the stretching vibration peaks of C-Br bond at 500–700 cm^{-1} are also observed on Bd molecule. Interestingly, these C-Br peaks disappear in CN/Bd, suggesting that the Br element may be involved in the polymerization with g-C_3N_4 during the synthesis of CN/Bd.

To further reveal the chemical states of samples, XPS analysis was performed and the characterization results were shown in Fig. 2**c–f**. The total spectrum shows that all samples (CN and CN/Bd) contain C, N, O elements. As shown in the C 1 s spectrum, the peaks at 288.12 eV and 288.30 eV were observed on CN and CN/Bd, respectively, corresponding to the (N-C = N) sp^2-hybridized carbon of the triazine ring. In the N 1 s spectrum, CN displays similar characteristic peaks to CN/Bd with 398.32 eV, 399.21 eV and 401.19 eV representing sp^2 hybridized N (C-N = C) in the triazine ring, sp^3 hybridized N (N-$(C)_3$) and unpolymerized -NH_X, respectively. As the electron-acceptor group, the introduction of Bd in the C 1 s and N 1 s spectra decreases the electron cloud density of the triazine ring, which increases the binding energy of CN/Bd [32]. This indicates the successful introduction of Bd and the strong interaction between CN and Bd, which may be conducive to enhancing electron transfer and promoting the reduction of O_2 to H_2O_2. Moreover, the peaks at 533.20 eV and 531.60 eV in the O1s spectrum are attributed to the adsorbed oxygen on the surface of catalysts and the C = O bond, respectively. Based on the above results and the decreased peak intensity of -NH_x, it is concluded that the amino group (–NH_2) of g-C_3N_4 reacts with the halogen group (-Br) in the Bd molecule through the C-N linkage. The oxygen content in CN and CN/Bd is 2.17% and 5.57%, respectively (Table S1), due to the presence of carbonyl group in the Bd molecule.

Titanium silicate-1 (TS-1) zeolite with partial replacement of Si by Ti is a critical catalyst for propylene epoxidation. To confirm the successful synthesis of TS-1, a series of characterizations were performed. As shown in Fig. S4**a**, XRD analysis shows the pure-silica zeolite molecular sieve structure of silicalite-1 (S-1) with a particle size range of 200–300 nm (Fig. S4**b**) [33]. Element mapping and EDX spectra analysis show no Ti element (0.01 wt%, probably due to instrumental error) was detected on S-1 (Fig. S4**c–e**). Noteworthily, TS-1 maintains the topology of the original MFI molecular sieve and similar particle size compared with S-1 (Fig. S5**a, b**) [34,35]. Moreover, a certain of Ti element (0.76 wt%) was uniformly dispersed on TS-1 (Fig. S5**c, d**), indicating the successful doping of Ti. FT-IR spectra analysis further demonstrate the successful replacement of Ti. A vibrational band at 960 cm^{-1} in the FT-IR spectra of TS-1 is attributed to the stretching vibration of Si–O–Ti bond in the framework (Fig. S6**a**) [36]. Further evidence comes from the UV–vis spectra analysis. An absorption peak of 205 nm attributed to tetrahedral-coordinated Ti species is observed on TS-1 compared with S-1 (Fig. S6**b**) [36]. And there is no extra-framework TiO_2, as evidenced by the absence of an absorption band at 330 nm [8,37]. The above chemical structure characterization confirms the successful synthesis of TS-1. Moreover, N_2 adsorption – desorption isotherms of TS-1 show that the Brunauer–Emmett–Teller surface area and pore volume of TS-1 are 397 $m^2 \cdot g^{-1}$ and 0.22 $cm^3 \cdot g^{-1}$, respectively (Fig. S7). This suggests that the larger surface area of TS-1 may be conducive to the adsorption activation of propylene substrate.

3.2. *Photocatalytic H_2O_2 and PO production*

In order to evaluate the photocatalytic activities of CN/Bd, photocatalytic production of H_2O_2 tests were conducted under saturated oxygen at room temperature with a blue light lamp (10 W, λ = 420–430 nm) as the light source, and a UV spectrophotometer was used to detect the product H_2O_2. Different precursors including melem, urea, dicyandiamide and melamine were selected to examine their catalytic effects under the same test conditions (Table S2**, entry 1–4**). The highest yield of H_2O_2 was obtained when melem as the precursor. Moreover, different types of sacrificial agents (methanol, ethanol and isopropanol) were screened (Table S2**, entry 1, 5, 6**). Compared with the common sacrificial agents (ethanol and isopropanol), methanol possesses the best performance with a high H_2O_2 yield of 9.41 $mmol \cdot g^{-1}$ at 7 h. In addition, the photocatalytic performance under blue light (10 W, λ = 420–430 nm) is nearly four times that of Xenon light (300 W) (Table S2**, entry 7**), which may be due to the better absorbance of CN/Bd around 420 nm. The control experiments (Table S2**, entry 8–10**) showed that no H_2O_2 is detected in the absence of catalyst and light, indicating that they are extremely important for the photocatalytic synthesis of H_2O_2.

The effect of ligand Bd addition amount on the H_2O_2 yield was investigated (Fig. 3**a**). Pristine CN exhibites a low H_2O_2 yield of 5.49 mmol·g^{-1} after reaction for 7 h, consistent with the severe charge recombination in pristine CN. After the introduction of Bd molecules, the catalytic performance is significantly improved. The highest yield (9.41 mmol·g^{-1}) of H_2O_2 is achieved over the optimized CN/Bd-7 catalyst, which is nearly twice that of pristine CN. However, CN/Bd-7 shows a low yield of 4.17 mmol·g^{-1} under air condition (Fig. 3**b**), which is about 50% of that under the O_2 condition. And almost no H_2O_2 is detected under argon, indicating the essential role of O_2 in the photocatalytic H_2O_2 production. Moreover, the catalytic performance at different intervals on CN/Bd-7 was studied (Fig. 3**c**). The yield of H_2O_2 increases linearly within 1 h and reach 3.51 mmol·g^{-1}·h^{-1}, exceeding most reported literatures (**Table S3**). The production rate of H_2O_2 decreases over time, probably due to the depletion of methanol and dissolved oxygen. Cycling tests were used to evaluate the photoactive stability of CN/Bd-7. As shown in Fig. 3**d**, CN/Bd exhibits preferable stability, and the catalytic performance has no significant decline even after 5 cycles.

In order to improve the utilization efficiency of H_2O_2 in propylene epoxidation reaction, TS-1 was used as the epoxidation catalyst to study the tandem process of photocatalytic generation of H_2O_2 and PO. The reaction conditions were the same as before, but TS-1 was added into reaction system. Fig. 3**a** indicates that the rate of H_2O_2 production plays a decisive role in PO production. With the increase of Bd molecule doping amount, the production rate of PO is consistent with that of H_2O_2, showing a volcanic trend. The maximum PO production is achieved when the doping amount of Bd is 7 mg (CN/Bd-7, doping ratio of 1:72). Therefore, the optimized CN/Bd-7 catalyst is screened for the propylene epoxidation reaction (CN/Bd in the latter refers to CN/Bd-7 if not otherwise specified). Further increasing the Bd content causes a decreased catalytic performance, possibly because the excessive doping of Bd seems to destroy the electronic structure of CN and hinder the light absorption ability of CN in the range of 250–450 nm [38,39], which are detrimental to photocatalytic H_2O_2 and PO production. Moreover, the tests results (Fig. 3**b**) under different reaction atmospheres show the PO production of O_2, Air and Ar are 8.244, 3.594 and 0.018 mmol·g^{-1} at 7 h, respectively. The difference in catalytic performance may be related to the concentration of O_2, indicating the importance of O_2 in PO production. Moreover, the production rate of PO is also consistent with that of H_2O_2, which further proves that the production of PO is related to the yield of H_2O_2 generated in situ.

The PO production was monitored at different reaction time. As shown in Fig. 4**a**, PO production gradually increases with the increase of reaction time. Noteworthily, the highest PO yield of 1.33 mmol·g^{-1}·h^{-1} is obtained at 6 h, followed by a gradual deceleration, possibly due to the consumption of oxygen/air and propylene in the reaction system. Moreover, the selectivity of main product PO is over 99% for the whole reaction, and no other by-products are detected by gas chromatographic and ^{1}H NMR tests (**Fig. S8**), except for a trace amount of acetone. In addition, based on the difference value between the amount of H_2O_2 produced (49.35 μmol) in the absence of TS-1 and the H_2O_2 remaining (9.40 μmol) after PO production, the consumption of H_2O_2 is calculated to 39.95 μmol at 6 h. Meanwhile, the production of PO is 39.93 μmol at 6 h. Thus, the utilization efficiency of H_2O_2 reached more than 95% at 6 h (Fig. 4**b**, Fig. 4**c**). Moreover, the yields of H_2O_2 and PO were basically the same at 6 h (**Fig. S9**), indicating that in situ-synthesized H_2O_2 could be efficiently used for PO production. At the initial stage of the reaction, the low utilization efficiency of H_2O_2 may be due to the low concentration of H_2O_2 generated in situ, which cannot effectively combine with TS-1 to participate in the formation of PO [40]. The PO yield did not decrease significantly after three cycles on the catalyst, which proves that the catalyst has good cycling stability (Fig. 4**d**).

In summary, the in-situ production of H_2O_2 for the propylene epoxidation reaction was achieved, which promoted the efficient utilization of H_2O_2. The PO yield was as high as 1.33 mmol·g^{-1}·h^{-1} with PO selectivity over 99%, exceeding most reported literatures (**Table S4**) and H_2O_2 utilization over 95%.

3.3. Photocatalytic mechanism

Series of mechanism investigations were carried out to explain the above experimental observations. The photochemical and photoelectrochemical properties of photocatalysts were obtained by UV–Vis DRS spectra, PL spectra, transient photocurrent responses and EIS plots. As shown in Fig. 5**a**, the light absorption capacity of CN is the poorest. With the doping amount of the ligand Bd, the maximum absorption edge of the photocatalyst is continuously extended, so that the CN/Bd has a

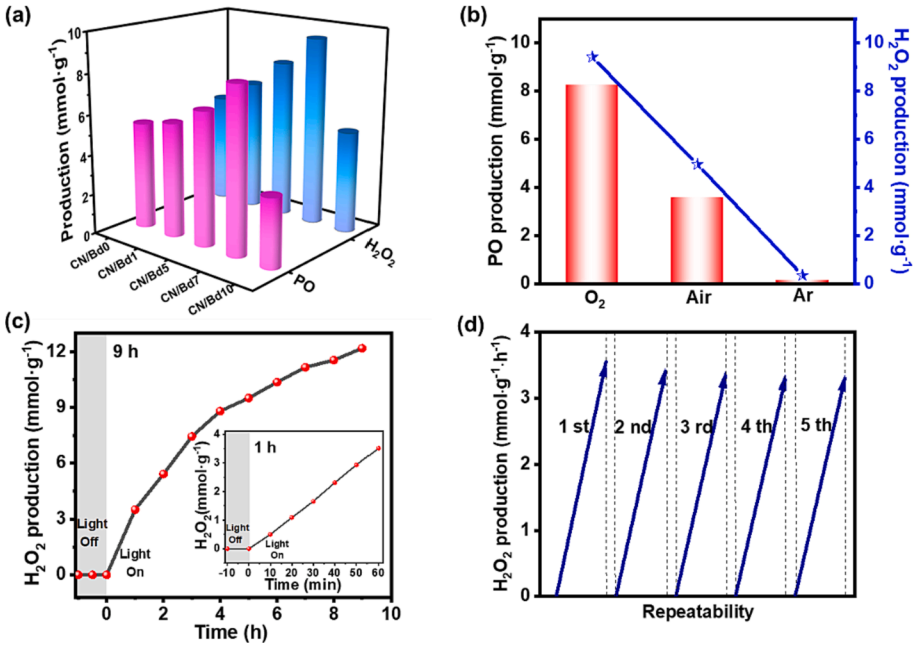

Fig. 3. The production of H_2O_2 and PO (a) under different Bd addition, (b) under different gas atmosphere; (c) the production of H_2O_2 with different reaction time on CN/Bd-7. Inset: H_2O_2 production rate for 1 h; (d) the cycle tests for CN/Bd-7.

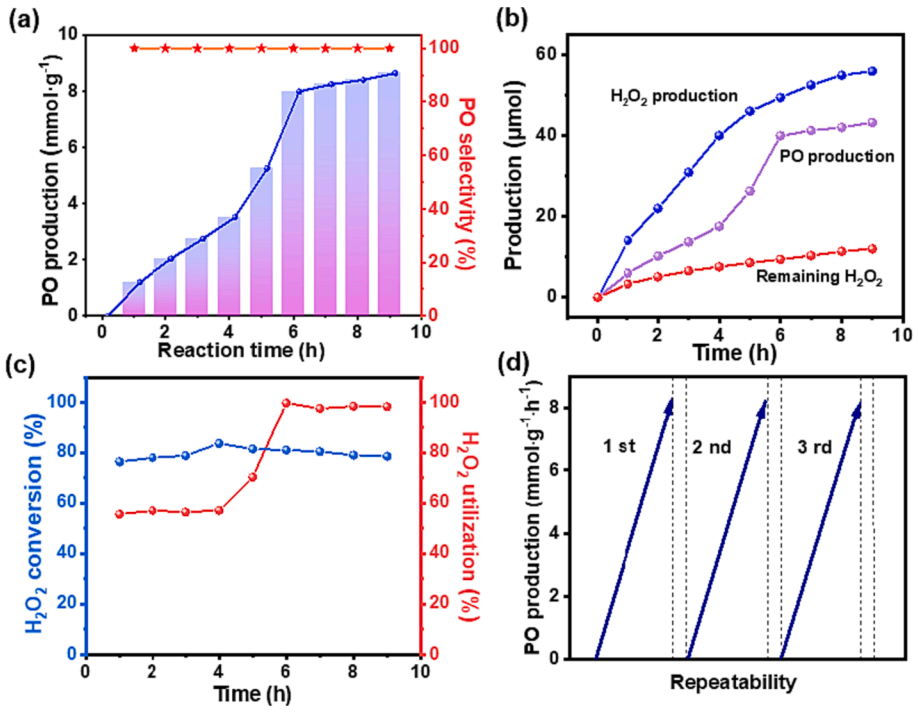

Fig. 4. (a) The production and selectivity of PO, (b) H_2O_2 and PO production and remaining H_2O_2 after the reaction, (c) the conversion and utilization efficiency of H_2O_2, (d) the PO cycle test results for CN/Bd-7.

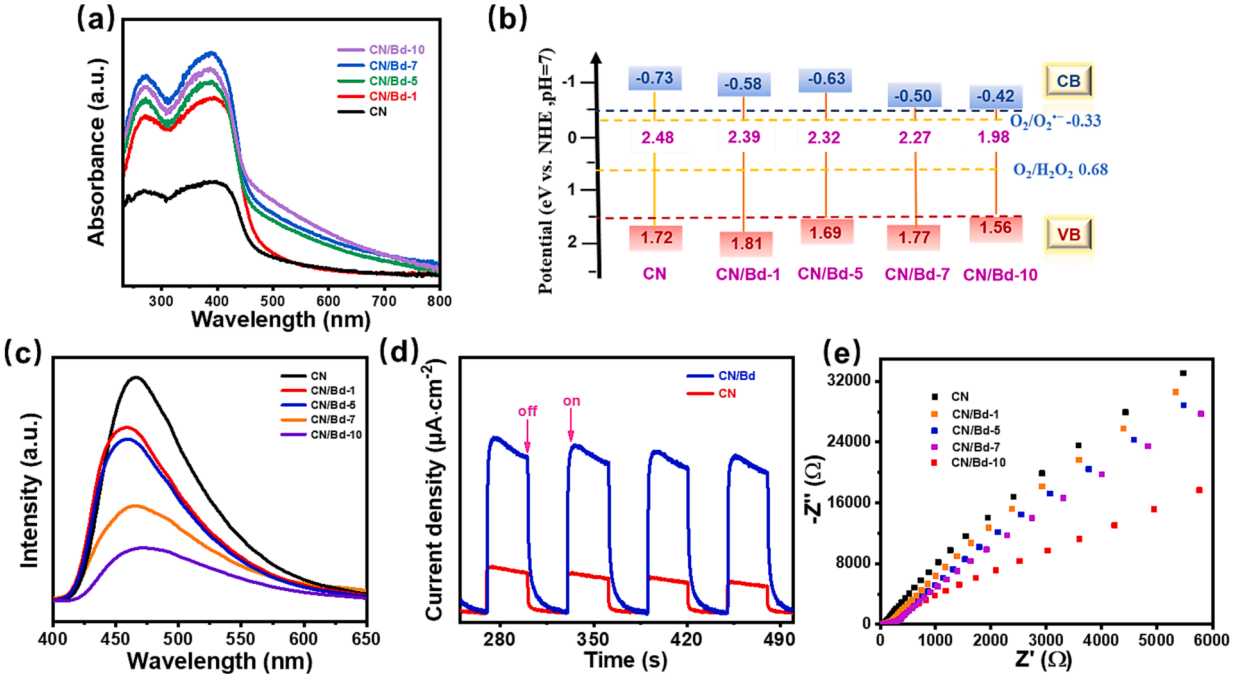

Fig. 5. (a) UV–Vis diffuse reflection spectrum of CN/Bd-X, (b) conduction band and valence band value of CN and CN/Bd-X, (c) PL spectra of CN/Bd-X, (d) transient photocurrent response curves of CN and CN/Bd-7, (e) electrochemical impedance curves of CN/Bd-X.

much higher utilization of the available light than normal CN. Bandgaps of these samples were determined from the transformed Kubelka-Munk function. Compared to CN, the CN/Bd optical energy gap is reduced from 2.48 eV to 2.27 eV (Fig. S10). In addition, for CN/Bd, the conduction band (CB) value is −0.50 V, lower than −0.33 V ($E(O_2/O_2^{\bullet-})$ = -0.33 V vs. NHE), and the valence band (VB) value is 1.77 V, higher than 0.68 V ($E(O_2/H_2O_2)$ = 0.68 V vs. NHE). Therefore, the excellent visible light absorption capacity and suitable bandgap position show that the CN/Bd has great theoretical potential in the photocatalytic reduction reaction of O_2 to H_2O_2 (Fig. 5**b and** S11). PL spectra were examined to explore the transfer, recombination and utilization of photo-generated carriers in samples. As illustrated in Fig. 5**c**, the PL emission intensity of CN/Bd is decreased significantly after doping with appropriate amount of ligands, which suggests that Bd doping is more effective for the separation of photogenerated electron-hole pairs [41]. This conclusion is also confirmed by the photoelectrochemical testing. As

shown in Fig. 5**d, e**, CN/Bd exhibits higher photo-current density and lower EIS radius compared with pristine CN, further confirming the excellent optical and electrical properties of CN/Bd: more efficient separation and migration of photogenerated electron-hole [42].

There are two pathways for the photocatalytic synthesis of H_2O_2, including the O_2 reduction pathway and the H_2O oxidation pathway [43]. As shown in (**Table S2 entry 11**), almost no H_2O_2 was detected under argon atmosphere and pure water on CN/Bd. This result suggests that H_2O_2 is produced from O_2 reduction rather than H_2O oxidation. In order to further investigate the reaction mechanism of CN/Bd in photocatalytic H_2O_2 synthesis, the linear scanning voltammetry (LSV) curves of CN/Bd at 400–1600 rpm were tested by rotating disk electrode in the O_2 saturation state (Fig. 6**a**). The average number (n) of electron transferred on CN/Bd during oxygen reduction reaction was obtained by fitting the Koutecky-Levich equation (Eq. (4). As shown in Fig. 6**b**, the n value for CN/Bd is calculated to be 1.8, confirming its $2e^-$-dominated oxygen reduction process, which further explained the strong production ability of H_2O_2 over CN/Bd.

$$\frac{1}{i}=\frac{1}{i_k}+\frac{1}{0.62nFD_0^{\frac{2}{3}}\vartheta^{-1/6}C_0}\times 1/\omega^{0.5} \quad (4)$$

In order to further explore the reactive oxygen species (ROS) in the reduction of O_2 to H_2O_2, ROS trapping experiments were performed. Para-Quinone (PBQ), silver nitrate ($AgNO_3$), 2,2,6,6-tetramethylpiperidine (TEMP), and ammonium oxalate ($(NH_4)_2C_2O_4$) were adopted as the scavengers of superoxide radicals ($O_2^{\bullet-}$), electron, singlet oxygen ($^1O_2$) and hole, respectively (Fig. 6**c**). The yield of H_2O_2 decreased slightly after the addition of $(NH_4)_2C_2O_4$, indicating hole had little effect on the formation of H_2O_2, and the water oxidation reaction path was further excluded. Compared with TEMP, H_2O_2 production decreased significantly after adding $AgNO_3$ and PBQ, demonstrating that the reaction was the oxygen reduction path. In particular, $O_2^{\bullet-}$ played a major role in the reaction, followed by e^-, while $^1O_2$ almost rarely worked. This further confirms the formation of H_2O_2 may undergo a two-step single-electron path.

To further reveal the formation mechanism for H_2O_2, the intermediates during the reaction were investigated. In situ electron paramagnetic resonance (EPR) with 5,5-dimethyl-1-pyrroline-N-oxide (DMPO) as the spin-trapping agent was performed to identify intermediate radicals, confirming the pathways of H_2O_2 generation. As shown in Fig. 6**d**, six prominent characteristic signals of DMPO − $O_2^{\bullet-}$ were detected under irradiation compared with dark conditions, suggesting that $O_2^{\bullet-}$ radicals may be the reactive oxygen species (ROS) during the reaction process [40]. Moreover, CN/Bd exhibites a stronger signal of DMPO − $O_2^{\bullet-}$ than pristine CN, indicating that the photogenerated electrons of CN/Bd possessed superior reductive ability to reduce O_2 by taking one electron to form $O_2^{\bullet-}$. The above results reveal that the production of H_2O_2 may undergo two-step single-electron ORR process, consistent with the ROS trapping experiments results.

Based on the above experimental results, the mechanism of H_2O_2 generation on CN/Bd is reasonably speculated (Fig. 7). Under visible light irradiation, abundant electrons (e^-) are generated and excited to conduction band (CB) of CN/Bd, while holes (h^+) remain on valence band (VB). Next, h^+ oxidize methanol to release H^+ protons (Eq. (5), and O_2 is reduced to $O_2^{\bullet-}$ by single electron (e^-) on CB (Eq. (6). The reduction potential value of CN/Bd is −0.5 eV, more negative than that of $O_2/O_2^{\bullet-}$(-0.33 V), proving the feasibility of H_2O_2 generation via oxygen reduction pathway on CN/Bd. The generated $O_2^{\bullet-}$ reacts with H^+ to produce $^\bullet$OOH radicals (Eq. (7), which in turn reacts with another electron to produce HO_2^- anion (Eq. (8). Finally, HO_2^- reacts with H^+ to produce the final H_2O_2 product according to Eq. (9). In summary, the proposed photocatalytic H_2O_2 production mechanism on CN/Bd adopts the two-step single-electron oxygen reduction pathway.

$$CH_3OH + h^+ \rightarrow HCHO + 2H^+ \quad (5)$$

$$O_2 + e^- \rightarrow O_2^{\bullet-} \quad (6)$$

$$O_2^{\bullet-} + H^+ \rightarrow {}^\bullet OOH \quad (7)$$

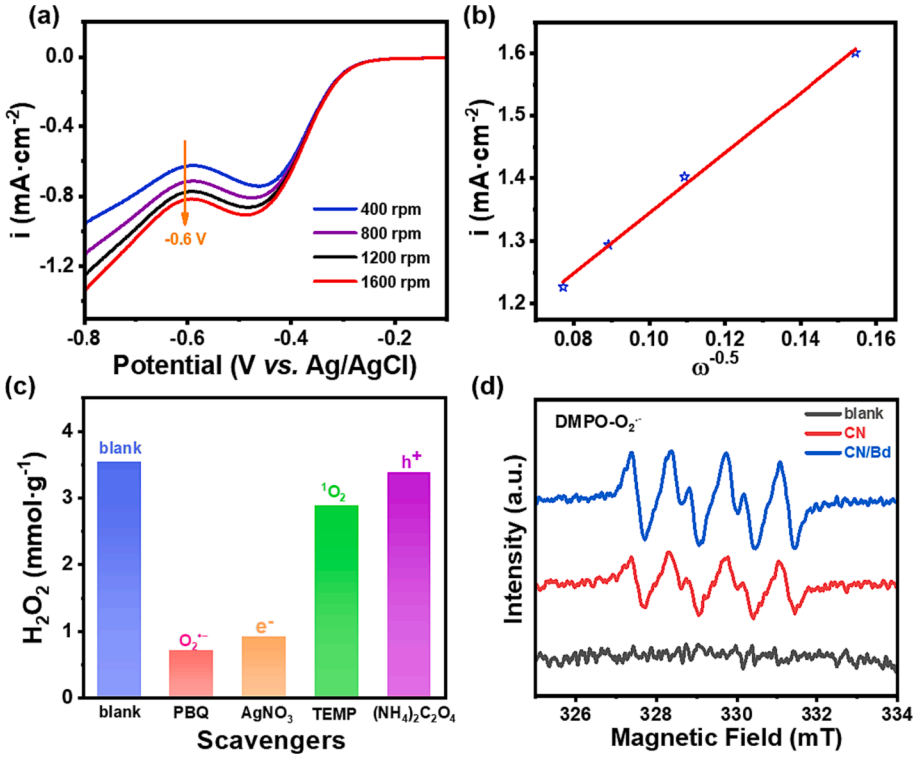

Fig. 6. (a) LSV of CN/Bd in O_2 saturated 0.1 M KOH at different rotating speeds, (b) Koutecky-Levich plots of the CN/Bd vs. Ag/AgCl at −0.6 V, (c) reactive oxygen species contributions of H_2O_2 production on CN/Bd and (d) comparison of EPR signals of CN and CN/Bd in the presence of DMPO after 10 min of light.

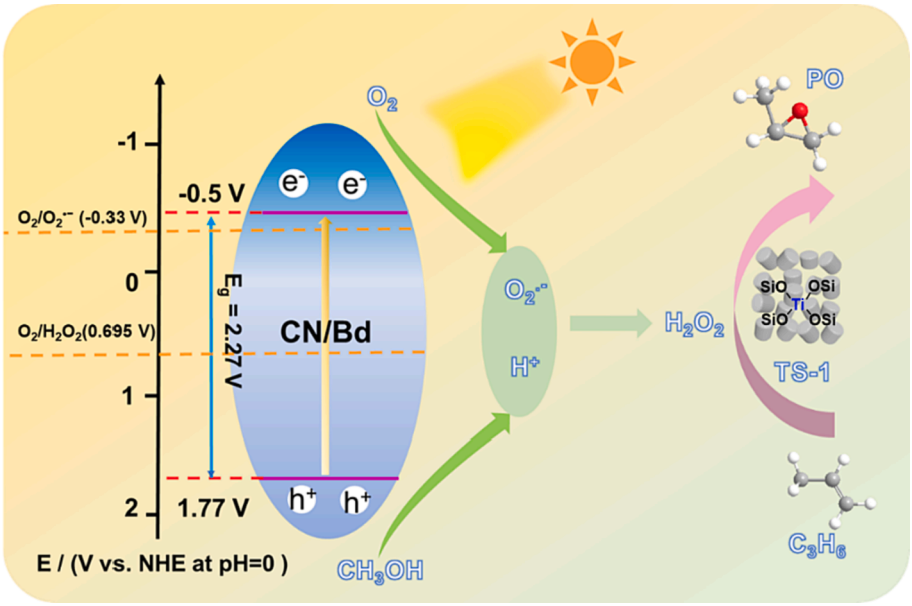

Fig. 7. Reaction mechanism diagram of the photocatalytic synthesis of H_2O_2 and PO on CN/Bd and TS-1.

$$^{\bullet}OOH + e^- \rightarrow HO_2^- \quad (8)$$

$$HO_2^- + H^+ \rightarrow H_2O_2 \quad (9)$$

Based on the above results, a plausible reaction mechanism on the generation of PO and by-products on TS-1 was depicted in **Scheme S1 and Scheme S2.** Firstly, H_2O_2 synthesized in situ on CN/Bd catalyst is absorbed on TS-1 (**Step I**) and then activated to form Ti-OOH (**Step II**), an active species of titanium peroxide. Subsequently, propylene is adsorbed at the Ti^{4+} site (**Step III**) and reacts with Ti-OOH to form PO and H_2O, and desorb from the Ti^{4+} site to complete the reaction cycle (**Step IV-V**) [44–49]. In addition, various kinds of side reactions (**Scheme S2**) may occur in the process of PO production. For example, propylene can be oxidized into acrolein. Moreover, the as-obtained PO products can also be ring-opened to generate propylene glycol, acetone, propanal and other by-products [46]. However, the production of these by-products may be more likely to occur under high temperatures, high pressures or other harsh conditions [10,36,50]. In this work, H_2O_2 is synthesized in situ on CN/Bd by photocatalysis with blue lamp (10 W, λ = 420–430 nm) as light source, and reacts with TS-1 to produce PO under ambient conditions. The mild conditions of the whole reaction process ensure the efficient and selective generation of PO, and almost no by-products are detected.

4. Conclusion

In conclusion, we propose a tandem strategy for the production of PO using photocatalytic in situ-synthesized H_2O_2. The CN/Bd is prepared by introducing the electron-acceptor Bd group and applied to photocatalytic synthesis of H_2O_2. For the propylene epoxidation reaction under ambient conditions, a high PO yield of 1.33 $mmol \cdot g^{-1} \cdot h^{-1}$ is achieved on TS-1 with high PO selectivity of over 99%, and the H_2O_2 utilization efficiency of over 95%. The proposed system enables PO production with O_2 as the oxidizing agent through the in situ-synthesized of H_2O_2 under light irradiation without using H_2 or expensive reagents, improving the H_2O_2 utilization and solving the problems of storage and transportation. This work not only provides a safer and more economical method for industrial PO production, but also provides guidance for in-situ utilization of H_2O_2.

Declaration of Competing Interest

The authors declare that they have no known competing financial interests or personal relationships that could have appeared to influence the work reported in this paper.

Data availability

Data will be made available on request.

Acknowledgements

This work was supported by National Key Research and Development Program of China (NO. 2019YFA0708700), National Natural Science Foundation of China (22179146, 51672309, 51172285 and 51372277), the Major Scientific and Technological Innovation Project of Shandong Province (2020CXGC010402), the Fundamental Research Funds for Central Universities (18CX07009A), YanKuang Group Co., Ltd. (YKZB2020-167), the Young Taishan Scholar Program of Shandong Province (tsqn20182027), Taishan Scholar Project (No. ts201712020) and the Technological Leading Scholar of 10000 Talent Project (W03020508).

Appendix A. Supplementary data

Supplementary data to this article can be found online at https://doi.org/10.1016/j.cej.2023.146488.

References

[1] Z. Song, X. Feng, N. Sheng, D. Lin, Y. Li, Y. Liu, X. Chen, D. Chen, X. Zhou, C. Yang, Cost-efficient core-shell TS-1/silicalite-1 supported Au catalysts: towards enhanced stability for propene epoxidation with H_2 and O_2, Chem. Eng. J. 377 (2019), 119927, https://doi.org/10.1016/j.cej.2018.09.088.

[2] L. Wang, J. Dai, Y. Xu, Y. Hong, J. Huang, D. Sun, Q. Li, Titanium silicalite-1 zeolite encapsulating Au particles as a catalyst for vapor phase propylene epoxidation with H_2/O_2: a matter of Au–Ti synergic interaction, J. Mater. Chem. A 8 (8) (2020) 4428–4436, https://doi.org/10.1039/c9ta12470e.

[3] W. Xiong, X.K. Gu, Z. Zhang, P. Chai, Y. Zang, Z. Yu, D. Li, H. Zhang, Z. Liu, W. Huang, Fine cubic Cu_2O nanocrystals as highly selective catalyst for propylene epoxidation with molecular oxygen, Nat. Commun. 12 (1) (2021) 5921, https://doi.org/10.1038/s41467-021-26257-0.

[4] Z. Zhang, Y. Tang, W. Du, J. Xu, Q. Wang, N. Song, G. Qian, X. Duan, X. Zhou, Engineering gold impregnated uncalcined TS-1 to boost catalytic formation of propylene oxide, Appl. Catal. B Environ. 319 (2022), 121837, https://doi.org/10.1016/j.apcatb.2022.121837.

[5] J. Ke, J. Zhao, M. Chi, M. Wang, X. Kong, Q. Chang, W. Zhou, C. Long, J. Zeng, Z. Geng, Facet-dependent electrooxidation of propylene into propylene oxide over

Ag_3PO_4 crystals, Nat. Commun. 13 (1) (2022) 932, https://doi.org/10.1038/s41467-022-28516-0.
[6] W. Li, G. Wu, W. Hu, J. Dang, C. Wang, X. Weng, I. da Silva, P. Manuel, S. Yang, N. Guan, L. Li, Direct propylene epoxidation with molecular oxygen over cobalt-containing zeolites, J. Am. Chem. Soc. 144 (9) (2022) 4260–4268, https://doi.org/10.1021/jacs.2c00792.
[7] J. Teržan, M. Huš, B. Likozar, P. Djinović, Propylene epoxidation using molecular oxygen over copper- and silver-based catalysts: a review, ACS Catal. 10 (22) (2020) 13415–13436, https://doi.org/10.1021/acscatal.0c03340.
[8] C.P. Gordon, H. Engler, A.S. Tragl, M. Plodinec, T. Lunkenbein, A. Berkessel, J. H. Teles, A.N. Parvulescu, C. Coperet, Efficient epoxidation over dinuclear sites in titanium silicalite-1, Nature 586 (7831) (2020) 708–713, https://doi.org/10.1038/s41586-020-2826-3.
[9] C. Samanta, Direct synthesis of hydrogen peroxide from hydrogen and oxygen: an overview of recent developments in the process, Appl. Catal. A 350 (2) (2008) 133–149, https://doi.org/10.1016/j.apcata.2008.07.043.
[10] G. Wu, Y. Wang, L. Wang, W. Feng, H. Shi, Y. Lin, T. Zhang, X. Jin, S. Wang, X. Wu, P. Yao, Epoxidation of propylene with H_2O_2 catalyzed by supported TS-1 catalyst in a fixed-bed reactor: experiments and kinetics, Chem. Eng. J. 215–216 (2013) 306–314, https://doi.org/10.1016/j.cej.2012.11.055.
[11] B. Yu, T. Ayvalı, Z.-Q. Wang, X.-Q. Gong, A.A. Bagabas, S.C.E. Tsang, Gas phase selective propylene epoxidation over La_2O_3-supported cubic silver nanoparticles, Cat. Sci. Technol. 9 (13) (2019) 3435–3444, https://doi.org/10.1039/c9cy00567f.
[12] L.-L. Guo, J. Yu, W.-W. Wang, J.-X. Liu, H.-C. Guo, C. Ma, C.-J. Jia, J.-X. Chen, R. Si, Small-sized cuprous oxide species on silica boost acrolein formation via selective oxidation of propylene, Chinese J. Catal. 42 (2) (2021) 310–319, https://doi.org/10.1016/s1872-2067(20)63636-1.
[13] X. Feng, J. Yang, X. Duan, Y. Cao, B. Chen, W. Chen, D. Lin, G. Qian, D. Chen, C. Yang, X. Zhou, Enhanced catalytic performance for propene epoxidation with H_2 and O_2 over bimetallic Au–Ag/uncalcined titanium silicate-1 catalysts, ACS Catal. 8 (9) (2018) 7799–7808, https://doi.org/10.1021/acscatal.8b01324.
[14] Z. Zhu, H. Pan, M. Murugananthan, J. Gong, Y. Zhang, Visible light-driven photocatalytically active g-C_3N_4 material for enhanced generation of H_2O_2, Appl. Catal. B Environ. 232 (2018) 19–25, https://doi.org/10.1016/j.apcatb.2018.03.035.
[15] Y. Sun, L. Han, P. Strasser, A comparative perspective of electrochemical and photochemical approaches for catalytic H_2O_2 production, Chem. Soc. Rev. 49 (18) (2020) 6605–6631, https://doi.org/10.1039/d0cs00458h.
[16] Y. Shiraishi, T. Takii, T. Hagi, S. Mori, Y. Kofuji, Y. Kitagawa, S. Tanaka, S. Ichikawa, T. Hirai, Resorcinol-formaldehyde resins as metal-free semiconductor photocatalysts for solar-to-hydrogen peroxide energy conversion, Nat. Mater. 18 (9) (2019) 985–993, https://doi.org/10.1038/s41563-019-0398-0.
[17] Y. Shiraishi, M. Matsumoto, S. Ichikawa, S. Tanaka, T. Hirai, Polythiophene-doped resorcinol-formaldehyde resin photocatalysts for solar-to-hydrogen peroxide energy conversion, J. Am. Chem. Soc. 143 (32) (2021) 12590–12599, https://doi.org/10.1021/jacs.1c04622.
[18] H. Zhao, Q. Jin, M.A. Khan, S. Larter, S. Siahrostami, M.G. Kibria, J. Hu, Rational design of carbon nitride for remarkable photocatalytic H_2O_2 production, Chem Catal. 2 (7) (2022) 1720–1733, https://doi.org/10.1016/j.checat.2022.04.015.
[19] H. Hou, X. Zeng, X. Zhang, Production of hydrogen peroxide by photocatalytic processes, Angew. Chem. Int. Ed. 59 (40) (2020) 17356–17376, https://doi.org/10.1002/anie.201911609.
[20] J. Zhang, L. Zheng, F. Wang, C. Chen, H. Wu, S.A.K. Leghari, M. Long, The critical role of furfural alcohol in photocatalytic H_2O_2 production on TiO_2, Appl. Catal. B Environ. 269 (2020), 118770, https://doi.org/10.1016/j.apcatb.2020.118770.
[21] K. Kim, J. Park, H. Kim, G.Y. Jung, M.-G. Kim, Solid-phase photocatalysts: physical vapor deposition of Au nanoislands on porous TiO_2 films for millimolar H_2O_2 production within a few minutes, ACS Catal. 9 (10) (2019) 9206–9211, https://doi.org/10.1021/acscatal.9b02269.
[22] Y. Shiraishi, Y. Kofuji, H. Sakamoto, S. Tanaka, S. Ichikawa, T. Hirai, Effects of surface defects on photocatalytic H_2O_2 production by mesoporous graphitic carbon nitride under visible light irradiation, ACS Catal. 5 (5) (2015) 3058–3066, https://doi.org/10.1021/acscatal.5b00408.
[23] H. Ou, P. Yang, L. Lin, M. Anpo, X. Wang, Carbon nitride aerogels for the photoredox conversion of water, Angew. Chem. Int. Ed. 56 (36) (2017) 10905–10910, https://doi.org/10.1002/anie.201705926.
[24] H. Hirakawa, S. Shiota, Y. Shiraishi, H. Sakamoto, S. Ichikawa, T. Hirai, Au Nanoparticles supported on $BiVO_4$: effective inorganic photocatalysts for H_2O_2 production from water and O_2 under visible light, ACS Catal. 6 (8) (2016) 4976–4982, https://doi.org/10.1021/acscatal.6b01187.
[25] D. Lin, Q. Zhang, Z. Qin, Q. Li, X. Feng, Z. Song, Z. Cai, Y. Liu, X. Chen, D. Chen, S. Mintova, C. Yang, Reversing titanium oligomer formation towards high-efficiency and green synthesis of titanium-containing molecular sieves, Angew. Chem. Int. Ed. 60 (7) (2021) 3443–3448, https://doi.org/10.1002/anie.202011821.
[26] Y. Xing, Z. Yao, W. Li, W. Wu, X. Lu, J. Tian, Z. Li, H. Hu, M. Wu, Fe/Fe_3C Boosts H_2O_2 utilization for methane conversion overwhelming O_2 generation, Angew. Chem. Int. Ed. 60 (16) (2021) 8889–8895, https://doi.org/10.1002/anie.202016888.
[27] L. Chen, C. Chen, Z. Yang, S. Li, C. Chu, B. Chen, Simultaneously tuning band structure and oxygen reduction pathway toward high-efficient photocatalytic hydrogen peroxide production using cyano-rich graphitic carbon nitride, Adv. Funct. Mater. 31 (46) (2021) 2105731, https://doi.org/10.1002/adfm.202105731.
[28] S. Li, G. Dong, R. Hailili, L. Yang, Y. Li, F. Wang, Y. Zeng, C. Wang, Effective photocatalytic H_2O_2 production under visible light irradiation at g-C_3N_4 modulated by carbon vacancies, Appl. Catal. B Environ. 190 (2016) 26–35, https://doi.org/10.1016/j.apcatb.2016.03.004.
[29] F. Wang, J. Xu, Z. Wang, Y. Lou, C. Pan, Y. Zhu, Unprecedentedly efficient mineralization performance of photocatalysis-self-Fenton system towards organic pollutants over oxygen-doped porous g-C_3N_4 nanosheets, Appl. Catal. B Environ. 312 (2022), 121438, https://doi.org/10.1016/j.apcatb.2022.121438.
[30] L. Xu, L. Li, Z. Hu, J.C. Yu, Boosting alkaline photocatalytic H_2O_2 generation by incorporating pyrophosphate on g-C_3N_4 for effective proton shuttle and oxygen activation, Appl. Catal. B Environ. 328 (2023), 122490, https://doi.org/10.1016/j.apcatb.2023.122490.
[31] G. Liu, G. Zhao, W. Zhou, Y. Liu, H. Pang, H. Zhang, D. Hao, X. Meng, P. Li, T. Kako, J. Ye, In situ bond modulation of graphitic carbon nitride to construct p-n homojunctions for enhanced photocatalytic hydrogen production, Adv. Funct. Mater. 26 (37) (2016) 6822–6829, https://doi.org/10.1002/adfm.201602779.
[32] L. Zhou, J. Lei, F. Wang, L. Wang, M.R. Hoffmann, Y. Liu, S.-I. In, J. Zhang, Carbon nitride nanotubes with in situ grafted hydroxyl groups for highly efficient spontaneous H_2O_2 production, Appl. Catal. B Environ. 288 (2021), 119993, https://doi.org/10.1016/j.apcatb.2021.119993.
[33] X. Wei, J. Cheng, Y. Li, K. Cheng, F. Sun, Q. Zhang, Y. Wang, Bimetallic clusters confined inside silicalite-1 for stable propane dehydrogenation, Nano Res. 16 (8) (2023) 10881–10889, https://doi.org/10.1007/s12274-023-5953-y.
[34] M. Ko, Y. Kim, J. Woo, B. Lee, R. Mehrotra, P. Sharma, J. Kim, S.W. Hwang, H. Y. Jeong, H. Lim, S.H. Joo, J.-W. Jang, J.H. Kwak, Direct propylene epoxidation with oxygen using a photo-electro-heterogeneous catalytic system, Nat. Catal. 5 (1) (2021) 37–44, https://doi.org/10.1038/s41929-021-00724-9.
[35] J. Dai, W. Zhong, W. Yi, M. Liu, L. Mao, Q. Xu, D. Yin, Bifunctional H_2WO_4/TS-1 catalysts for direct conversion of cyclohexane to adipic acid: active sites and reaction steps, Appl. Catal. B Environ. 192 (2016) 325–341, https://doi.org/10.1016/j.apcatb.2016.04.005.
[36] W. Li, L. Chen, M. Qiu, W. Li, Y. Zhang, Y. Zhu, J. Li, X. Chen, Highly efficient epoxidation of propylene with in situ-generated H_2O_2 over a hierarchical TS-1 zeolite-supported non-noble nickel catalyst, ACS Catal. 13 (15) (2023) 10487–10499, https://doi.org/10.1021/acscatal.3c02206.
[37] W. Xu, T. Zhang, R. Bai, P. Zhang, J. Yu, A one-step rapid synthesis of TS-1 zeolites with highly catalytically active mononuclear TiO_6 species, J. Mater. Chem. A 8 (19) (2020) 9677–9683, https://doi.org/10.1039/c9ta13851j.
[38] J. Zhang, M. Zhang, S. Lin, X. Fu, X. Wang, Molecular doping of carbon nitride photocatalysts with tunable bandgap and enhanced activity, J. Catal. 310 (2014) 24–30, https://doi.org/10.1016/j.jcat.2013.01.008.
[39] L. Yang, G. Dong, D.L. Jacobs, Y. Wang, L. Zang, C. Wang, Two-channel photocatalytic production of H_2O_2 over g-C_3N_4 nanosheets modified with perylene imides, J. Catal. 352 (2017) 274–281, https://doi.org/10.1016/j.jcat.2017.05.010.
[40] B. An, Q.H. Zhang, B.S. Zheng, M. Li, Y.Y. Xi, X. Jin, S. Xue, Z.T. Li, M.B. Wu, W. T. Wu, Sulfone-decorated conjugated organic polymers activate oxygen for photocatalytic methane conversion, Angew. Chem. Int. Ed. 61 (28) (2022) e202204661.
[41] L. Zhou, Y. Tian, J. Lei, L. Wang, Y. Liu, J. Zhang, Self-modification of g-C_3N_4 with its quantum dots for enhanced photocatalytic activity, Cat. Sci. Technol. 8 (10) (2018) 2617–2623, https://doi.org/10.1039/c8cy00351c.
[42] M. Kou, Y. Wang, Y. Xu, L. Ye, Y. Huang, B. Jia, H. Li, J. Ren, Y. Deng, J. Chen, Y. Zhou, K. Lei, L. Wang, W. Liu, H. Huang, T. Ma, Molecularly engineered covalent organic frameworks for hydrogen peroxide photosynthesis, Angew. Chem. Int. Ed. 61 (19) (2022) e202200413.
[43] Z. Haider, H.-I. Cho, G.-H. Moon, H.-I. Kim, Minireview: selective production of hydrogen peroxide as a clean oxidant over structurally tailored carbon nitride photocatalysts, Catal. Today 335 (2019) 55–64, https://doi.org/10.1016/j.cattod.2018.11.067.
[44] X. Feng, D. Lin, D. Chen, C. Yang, Rationally constructed Ti sites of TS-1 for epoxidation reactions, Sci. Bull. 66 (19) (2021) 1945–1949, https://doi.org/10.1016/j.scib.2021.05.020.
[45] Y.Z. Peng, G.C. Guo, S. Guo, L.H. Kong, T.B. Lu, Z.M. Zhang, Charge transfer from donor to acceptor in conjugated microporous polymer for enhanced photosensitization, Angew. Chem. Int. Ed. 60 (40) (2021) 22062–22069, https://doi.org/10.1002/anie.202109968.
[46] Y. Liu, C. Zhao, B. Sun, H. Zhu, W. Xu, Preparation and modification of Au/TS-1 catalyst in the direct epoxidation of propylene with H_2 and O_2, Appl. Catal. A 624 (2021), 118329, https://doi.org/10.1016/j.apcata.2021.118329.
[47] D.T. Bregante, J.Z. Tan, R.L. Schultz, E.Z. Ayla, D.S. Potts, C. Torres, D.W. Flaherty, Catalytic consequences of oxidant, alkene, and pore structures on alkene epoxidations within titanium silicates, ACS Catal. 10 (17) (2020) 10169–10184, https://doi.org/10.1021/acscatal.0c02183.
[48] Z. He, Q. Lei, W. Dai, H. Zhang, Solvent tunes the selectivity of alkenes epoxidation over Ti-Beta Zeolite: a systematic kinetic assessment on elementary steps, kinetically relevant and reaction barriers, J. Catal. 421 (2023) 172–184, https://doi.org/10.1016/j.jcat.2023.03.012.
[49] J.J. Bravo-Suárez, K.K. Bando, J. Lu, M. Haruta, T. Fujitani, S.T. Oyama, Transient technique for identification of true reaction intermediates: hydroperoxide species in propylene epoxidation on gold/titanosilicate catalysts by x-ray absorption fine structure spectroscopy, J. Phys. Chem. C 112 (2008) 1115–1123.
[50] X. Lu, H. Wu, J. Jiang, M. He, P. Wu, Selective synthesis of propylene oxide through liquid-phase epoxidation of propylene with H_2O_2 over formed Ti-MWW catalyst, J. Catal. 342 (2016) 173–183, https://doi.org/10.1016/j.jcat.2016.07.020.